LAWRENCE
LIVERMORE
NATIONAL
LABORATORY

LLNL-CONF-454151

Satellite Collision Modeling with Physics-Based Hydrocodes: Debris Generation Predictions of the Iridium-Cosmos Collision Event and Other Impact Events

H. K. Springer, W. O. Miller, J. L. Levatin, A. J. Pertica, S. S. Olivier

September 9, 2010

AMOS Conference
Wailea, HI, United States
September 13, 2010 through September 17, 2010

Disclaimer

Satellite Collision Modeling with Physics-Based Hydrocodes: Debris Generation Predictions of the Iridium-Cosmos Collision Event and Other Impact Events

H. Keo Springer, Wayne O. Miller, JoAnne L. Levatin, Alex J. Pertica, Scot S. Olivier
Lawrence Livermore National Laboratory (LLNL)

ABSTRACT

Satellite collision debris poses risks to existing space assets and future space missions. Predictive models of debris generated from these hypervelocity collisions are critical for developing accurate space situational awareness tools and effective mitigation strategies. Hypervelocity collisions involve complex phenomenon that spans several time- and length-scales. We have developed a satellite collision debris modeling approach consisting of a Lagrangian hydrocode enriched with smooth particle hydrodynamics (SPH), advanced material failure models, detailed satellite mesh models, and massively parallel computers. These computational studies enable us to investigate the influence of satellite center-of-mass (CM) overlap and orientation, relative velocity, and material composition on the size, velocity, and material type distributions of collision debris.

We have applied our debris modeling capability to the recent Iridium 33-Cosmos 2251 collision event. While the relative velocity was well understood in this event, the degree of satellite CM overlap and orientation was ill-defined. In our simulations, we varied the collision CM overlap and orientation of the satellites from nearly maximum overlap to partial overlap on the outermost extents of the satellites (i.e, solar panels and gravity boom). As expected, we found that with increased satellite overlap, the overall debris cloud mass and momentum (transfer) increases, the average debris size decreases, and the debris velocity increases. The largest predicted debris can also provide insight into which satellite components were further removed from the impact location. A significant fraction of the momentum transfer is imparted to the smallest debris (< 1-5mm, dependent on mesh resolution), especially in large CM overlap simulations. While the inclusion of the smallest debris is critical to enforcing mass and momentum conservation in hydrocode simulations, there seems to be relatively little interest in their disposition. Based on comparing our results to observations, it is unlikely that the Iridium 33-Cosmos 2251 collision event was a large mass-overlap collision.

We also performed separate simulations studying the debris generated by the collision of 5 and 10 cm spherical projectiles on the Iridium 33 satellite at closing velocities of 5, 10, and 15 km/s. It is important to understand the vulnerability of satellites to small debris threats, given their pervasiveness in orbit. These studies can also be merged with probabilistic conjunction analysis to better understand the risk to space assets. In these computational studies, we found that momentum transfer, kinetic energy losses due to dissipative mechanisms (e.g., fracture), fragment number, and fragment velocity increases with increasing velocity for a fixed projectile size. For a fixed velocity, we found that the smaller projectile size more efficiently transfers momentum to the satellite. This latter point has an important implication: Eight (spaced) 5 cm debris objects can impart more momentum to the satellite, and likely cause more damage, than a single 10 cm debris object at the same velocity. Further studies are required to assess the satellite damage induced by 1-5 cm sized debris objects, as well as multiple debris objects, in this velocity range.

INTRODUCTION

On February 10, 2009, the privately-owned Iridium 33 satellite and the defunct Russian Cosmos 2251 satellite accidentally collided above northern Siberia, producing thousands of debris objects and further raising the possibility of future accidents. As Earth's orbit becomes more crowded, the frequency of such debris generation events can increase and, potentially, cascade into a runaway process called the Kessler Syndrome [1]. A high-fidelity space situational awareness (SSA) toolset is needed to develop effective mitigation strategies in order to circumvent such catastrophic scenarios. A critical component of this toolset is accurate debris generation modeling, whether for satellite-satellite, satellite-debris, or other orbital object collisions. The objective of this study is to use high-performance computing tools to investigate the influence of orbital object CM overlap, size, and relative velocity on the size and velocity distributions of the resultant debris. In doing so, we also develop models for debris size and velocity distributions, as well as debris scaling relationships for the satellite-sphere collisions.

MODEL DESCRIPTION

ParaDyn-SPH code and material models

Hypervelocity satellite collision simulations are performed using LLNL's explicit Lagrangian finite element analysis (FEA) code, ParaDyn (parallel DYNA3D [2]), enhanced with smooth particle hydrodynamics (SPH) [3]. The Lagrangian framework enables the optimum capturing of material interfaces during the transient collision phase, improving the accuracy of the simulated debris. The FEA-to-SPH conversion mechanism circumvents numerical issues in highly deformed regions, thereby maintaining simulation accuracy, particularly pressure-volume response, and computational efficiency. The collision simulations required up to 512 CPUs over 5 days and were performed on LLNL's Hera supercomputer (13,824 AMD Opteron 2.3 GHz Cores).

Fracture models are critical to the prediction of debris in these collision simulations. An advanced fracture model, MOSSFRAC [4], was utilized for the satellite materials. This model has been used previously in numerous simulations of hypervelocity impact problems. It features an orthogonal crack formation based on either shear or tensile criteria, Weibull statistical element seeding on crack formation criteria to represent material inhomogeneities necessary for "natural" fragmentation processes [5-7], as well as provisions for treatment of element strength when the crack is opened (loss of strength in crack direction under hydrostatic tension) or is closed (full strength under hydrostatic compression). In the MOSSFRAC model, the total strain increment tensor, $d\epsilon_{ij}$, is linearly partitioned into elastic (e), plastic (p), and crack (c) strain increments as shown below.

$$d\epsilon_{ij} = d\epsilon_{ij}^{e} + d\epsilon_{ij}^{p} + d\epsilon_{ij}^{c} \tag{1}$$

The elastic and plastic components are further separated into deviatoric and dilatational components as follows,

$$d\epsilon_{ij}^{e} = d\epsilon_{ij}^{e\,\prime} + d\epsilon_{ii}^{e}\delta_{ij} \tag{2}$$
$$d\epsilon_{ij}^{p} = d\epsilon_{ij}^{p\,\prime} + d\epsilon_{ii}^{p}\delta_{ij} = d\epsilon_{ij}^{p\,\prime} \text{ since } d\epsilon_{ii}^{p} \to 0 \text{ (plastic incompressibility)}$$

enabling the calculation of the deviatoric stress, given a strength model, and pressure, given an equation-of-state model. The formation of cracks in the MOSSFRAC model is based on a user-specified equivalent plastic strain to failure, $\bar{\epsilon}_{fail}$, and a spall strength, σ_{spall}. Table 1 lists the material parameters used in this study for the MOSSFRAC model.

A power-law strength model with pressure-dependent shear modulus [8] was used in these calculations,

$$Y = Y_0[1 + \beta\bar{\epsilon}]^n \tag{3}$$

where Y_0 is the initial yield strength, $\bar{\epsilon}$ ($d\bar{\epsilon} = \sqrt{\frac{2}{3}d\epsilon_{ij}^{p\,\prime}d\epsilon_{ij}^{p\,\prime}}$) is the equivalent plastic strain, and β and n are work hardening parameters. The von Mises (J2) yield condition was also used in this study to govern formation of plasticity where the equivalent stress is given by

$$\bar{\sigma} = \sqrt{\frac{3}{2}\sigma_{ij}'\sigma_{ij}'} \tag{4}$$

and σ_{ij}' is the deviatoric stress. If the equivalent stress is larger than the current yield stress in an element at a simulation time-step, then an incremental plastic strain is calculated. The overall plastic strain and the yield strength are then updated. Otherwise, the incremental plastic strain and yield strength are not updated, but the stress is still updated. There are no user-defined parameters for this model. A univariate polynomial equation-of-state model of the following form was also used to determine the material pressure-volume relationship

$$P = A_0 + A_1\mu + A_2\mu^2 + A_3\mu^3 + (B_0 + B_1\mu + B_2\mu^2)e \tag{5}$$

where A_i and B_i are the experimentally determined coefficients, e is the internal energy per volume, and μ is a volumetric parameter related to the dilatational component of the strain ($\mu = e^{-\frac{\epsilon_{ii}^e}{3}} - 1$). This parameter has the following characteristic: $\mu = 0$ under no load and $\mu > 0$ under compression. Table 1 lists the material parameters used in this study for the strength and equation-of-state models.

Table 1. Collision simulation material model parameters.

Material	ρ *(g/cc)*	Y_0 *(Mbar)*	β	n	A_i *(Mbar)*	B_i	$\bar{\epsilon}_{fail}$	σ_{spall} *(Mbar)*
Al 6061-T6	2.703	0.0029	125	0.1	0.0, 0.7419, 0.6049, 0.1871	1.970, 0.4800, 0.0	0.30	0.0080
Lead	11.34	0.00175	0.0	1.0	0.0, 0.4387, 0.4414, -0.105	2.74, 0.54, 0.0	0.3	0.003
Graphite epoxy composite	1.9	0.014	0.0	1.0	0.0, 0.1161, 0.1711, 0.0953	0.3, 0.0, 0.0	0.1	0.007
Aluminum honeycomb	0.35	0.0029	125	0.1	0.0, 0.7419, 0.6049, 0.1871	1.970, 0.4800, 0.0	0.30	0.0080

Also, a post-processor, DFRAG [9], was developed to extract key statistics from these simulations, including debris size, mass, velocity, angular velocity, inertia tensor, bounding box dimensions, and material composition. We employed a tightest fitting bounding box algorithm [11] and took the largest dimension to determine the debris length.

Iridium and Cosmos computational models

The Iridium and Cosmos computational mesh models were generated using Truegrid® and are shown in Figure 1. The Iridium geometry consisted of a bus (3.4 m long by 1.2 m wide), communication panels (3x) (each 1.86 m long by 0.86 m wide), and solar panels (2x) (each 3.39 m long by 1.15 m wide). The overall Iridium model mass was 577 kg. The Iridium mesh model was approximately 960,000 elements with an average element size of 1 cm. The Cosmos geometry consisted of a cylindrical main body (2 m diameter by 3 m long) with a gravity boom (6.5 m long). The main body was solar panels wrapped around the circumference and a cylinder representing internal components. The overall Cosmos model mass was 898 kg. The Cosmos mesh model was approximately 770,000 elements with an average element size of 1 cm.

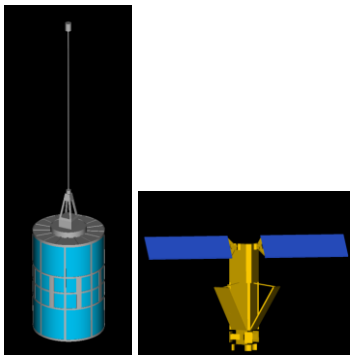

Figure 1. Computational models of the Iridium and Cosmos satellites used in the collision simulations.

Iridium-Cosmos and Iridium-sphere collision geometries

Several Iridium-Cosmos simulations were performed with different orientations and center-of-mass (CM) overlap, major collision uncertainties, to investigate the resultant debris trends. As an upper bound for debris generation response, a maximum CM overlap simulation was also performed. The closing velocity remained unchanged at 11.65 km/s in all these simulations. We also performed simulations of aluminum alloy (Al 6061-T6) spheres with 5 cm and 10 cm radii impacting the fixed Iridium satellite at 5, 10, and 15 km/s in order to investigate debris-induced satellite damage trends. In all these simulations, the aluminum spheres impacted the center of the Iridium bus.

RESULTS

Iridium-Cosmos collision modeling results

Figure 2 shows the progression of an Iridium-Cosmos collision simulation for the partial CM overlap case, i.e., glancing blow case. Simulations were performed in reference frame fixed to Cosmos, with the initial velocity vector given to the Iridium. At 0.6 ms, the Iridium solar panel and Cosmos gravity boom are cleanly sheared-off with a minimum of diffuse damage. In this respect, the formation of the solar panel and gravity boom debris is a semi-deterministic process governed by the geometry of the two satellites, as well as the collision geometry. In contrast at 10 ms, the impact of the Iridium communications panel causes relatively more diffuse damage in the main body of the Cosmos. This diffuse damage is due to the successive creation of debris from the initial impact location and continuing downstream through the Cosmos' thin, multi-layered structure. After 10 ms, the metrics associated with continued debris generation, relative debris velocity or velocity gradients within individual debris pieces, are generally small and not sufficient to create new debris.

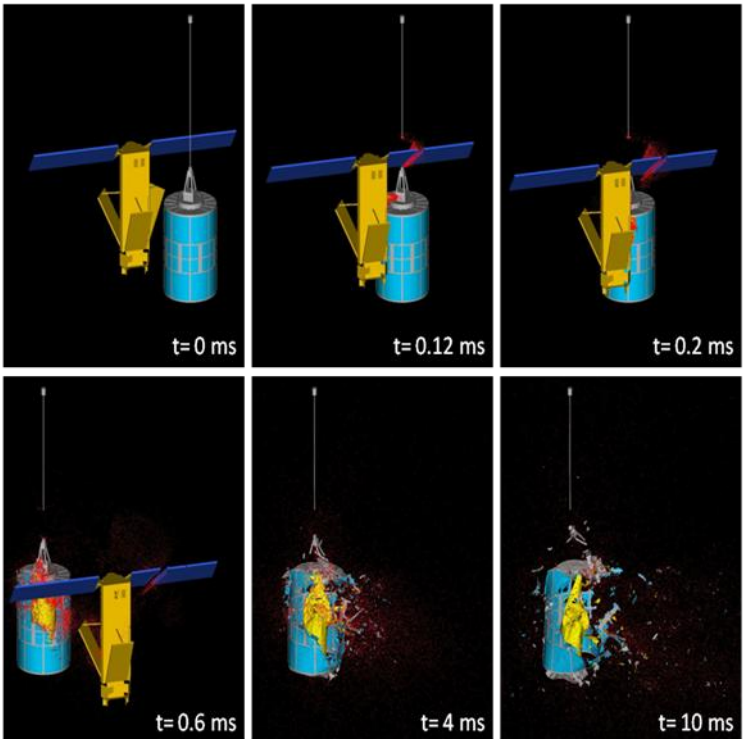

Figure 2. Progression of Iridium-Cosmos collision simulation (Glancing Blow Scenario #1, GB1). Newly created SPH particles are shown in red. In this configuration, the Iridium solar panel overlaps the Cosmos gravity boom and the Iridium communications panel overlaps the Cosmos main body. After 0.6 ms, the moving Iridium has left the field-of-view of the image (but still considered in the calculations)

Figure 3 shows the cumulative size distribution of the simulated debris for the various collision geometries. We considered four glancing blow (GB1-4) scenarios and a maximum overlap (MO) scenario in an attempt to bound the actual, but unknown, collision geometry and resultant debris. No attempt has been made to evaluate the likelihood of debris re-entry in this study and therefore the total predicted debris for each scenario is an upper bound. Comparisons are made to the published Cosmos 2251 RCS-based debris measurements of Liou [10]. The total debris number and power-law fits are shown in Table 2. We found that the total number of fragments predicted in the simulations (273-883 for GB1-4 and 5922 for MO scenarios, respectively) did bound the observed number of fragments (809). The prediction for GB4 (883) demonstrated the best agreement with the measurements (809). The momentum and kinetic energy transfer to the Cosmos, a metric of collision energy, scaled with the total predicted debris. This suggests that more debris results from higher energy collisions, which is observed in the debris prediction for MO scenario (5922). The largest predicted debris for all collision geometries (3.9 m to 4.5 m) were larger than the RCS-based measurements (approximately 2 m). This discrepancy may be related to the bounding box algorithm used to calculate the predicted debris size [11] and the method used to associate a debris size with RCS value [10]. Alternatively, the discrepancy may suggest that the GB scenarios in our simulations do not overlap the Cosmos gravity boom, the largest debris, as significantly as in the actual collision. We assert that the formation of the larger debris is deterministic in the collision of thin, single-layered structures since no cascading debris mechanisms are present. In this case, the debris is dependent on the initial satellite geometry and the construction, as well as the collision geometry. This is illustrated in the formation of the gravity boom debris and solar panel debris in Figure 2. This also suggests that it is critical to have accurate information about the satellites and the collision geometry in order to develop a good understanding of the largest debris. We also found that the cumulative debris length distribution obeyed a power-law trend overall ($N_{cum} = aL^b$), but that there are two distinct regions of the cumulative distribution curves most apparent in GB1-4 and the RCS-based measurements. At lower N_{cum} (<10), the initially higher power-law slope (b) flattens with increasing debris number; and then at higher N_{cum} (>10), b is nearly up to the maximum debris number. We fit a power-law to the overall cumulative distribution curve and to just a portion of the curve for the higher N_{cum} (>10). For these cases, the range of b for the higher N_{cum} (-1.24 to -2.82) are steeper than those for the overall cumulative distribution curve (-1.00 to -1.95). This is largely due to the flattening curve at lower N_{cum}. The power-law slope for the RCS-based Cosmos data is considerably steeper than those for either the GB1-4 or even the MO scenarios. This arises from the narrower debris size range for the RCS-based Cosmos debris (0.1 m to 2 m in length) compared to that of the predicted debris (0.02 m to 3-4 m). While the formation of the larger debris is a deterministic process governed by satellite and collision details, the formation of the smaller debris is a stochastic, but quantifiable, process dependent on the diffuse loading arising from impact on the multi-layered satellite. This induces an intrinsic material, or "natural", fragmentation response that has been studied extensively in metals [5-7].

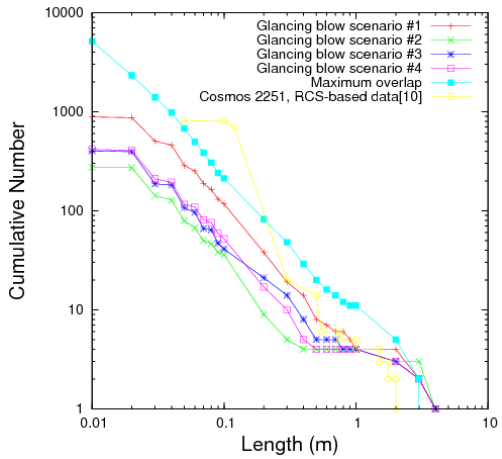

Figure 3. Predicted cumulative debris length distribution of the Cosmos 2251 for various glancing blow scenarios (GB1-4), as well as a maximum overlap (MO) scenario. Comparison is made with RCS-based data from Liou [10].

Table 2. Predicted Cosmos debris statistics for debris size greater than 1cm. Includes number of fragments (N_{tot}), average power-law fit parameters (a_{avg}, b_{avg}) and power-law fit parameters for only large N_{cum} (>20) (a_{hi}, b_{hi}) for various simulated collisions and RCS-based data [10].

Scenario	N_{tot}	a_{avg}	b_{avg}	a_{hi}	b_{hi}
Glancing Blow #1 (GB1)	883	5.14	-1.31	3.97	-1.43
Glancing Blow #2 (GB2)	273	3.43	-1.00	1.83	-1.27
Glancing Blow #3 (GB3)	402	3.93	-1.09	2.75	-1.24
Glancing Blow #4 (GB4)	415	3.59	-1.14	2.10	-1.36
Maximum Overlap (MO)	5922	9.15	-1.35	9.91	-1.32
RCS-based data[10]	809	4.92	-1.95	1.31	-2.82

Mass, momentum, and energy conservation laws can provide insight into the hypervelocity collisions and enable the development of predictive debris models. The ParaDyn-SPH code used for these simulations explicitly conserves mass and momentum. As part of analyzing these collision simulations, we have partitioned these fundamental quantities for larger (>1cm) and smaller (<1cm) Cosmos debris. This size threshold was related to orbital debris sensing capabilities. The conservation laws for a discrete system of debris are written as,

$$m_{cos} + m_{irid} = \overbrace{\sum_{i=1}^{N_{cos,debris>1cm}} m_i}^{m_{cosgt1}} + \overbrace{\sum_{i=1}^{N_{cos,debris<1cm}} m_i}^{m_{coslt1}} + \sum_{i=1}^{N_{irid}} m_i \quad (6)$$

$$m_{irid}\boldsymbol{v}_{irid} = \overbrace{\sum_{i=1}^{N_{cos,debris>1cm}} m_i\boldsymbol{v}_i}^{P_{cosgt1}} + \overbrace{\sum_{i=1}^{N_{cos,debris<1cm}} m_i\boldsymbol{v}_i}^{P_{coslt1}} + \overbrace{\sum_{i=1}^{N_{irid}} m_i\boldsymbol{v}_i}^{\mathrm{P_{irid}}} \quad (7)$$

$$\frac{1}{2}m_{irid}(\boldsymbol{v}_{irid}\cdot\boldsymbol{v}_{irid}) = \overbrace{\sum_{i=1}^{N_{cos,debris>1cm}} \frac{1}{2}m_i(\boldsymbol{v}_i\cdot\boldsymbol{v}_i)}^{KE_{cosgt1}} + \overbrace{\sum_{i=1}^{N_{cos,debris<1cm}} \frac{1}{2}m_i(\boldsymbol{v}_i\cdot\boldsymbol{v}_i)}^{KE_{coslt1}} + \overbrace{\sum_{i=1}^{N_{irid}} m_i\boldsymbol{v}_i}^{KE_{irid}} + E_{loss} \quad (8a)$$

$$E_{loss} = \overbrace{\sum_{i=1}^{N_{debris}} \int_{V_{debris,i}} p\,dV}^{p-V\ work} + \overbrace{\sum_{i=1}^{N_{debris}} \int_{V_{debris,i}} (\boldsymbol{\sigma}' : \boldsymbol{\varepsilon}^{\boldsymbol{pl}})\,dV}^{plastic\ work} + \overbrace{\sum_{i=1}^{N_{debris}} \int_{A_{debris,i}} \gamma_{fract}\,dA}^{fracture\ energy} \quad (8b)$$

where m is the mass, N is the debris number, $\boldsymbol{v}$ is the velocity vector, KE is the kinetic energy, p is the pressure, $\boldsymbol{\sigma}'$ is the deviatoric stress tensor, $\boldsymbol{\varepsilon^{pl}}$ is the plastic strain tensor, and γ_{fract} is the fracture energy per unit area. The rotational energy is small and has been neglected. The predicted Cosmos debris mass, momentum, and kinetic energy for debris greater than and less than 1 cm in size are shown in Table 3. We found that $m_{coslt1} < m_{cosgt1}$ for the GB cases, but $m_{coslt1} > m_{cosgt1}$ for the MO case. Minimal CM overlap on the Cosmos in the GB cases minimizes the collision damage and, thus, m_{coslt1}. In contrast, the CM overlap on the Cosmos in the MO case, by definition, maximizes the collision damage and production of small debris. It should be noted that the SPH particles comprised most of the debris less than 1 cm in size. Momentum transfer is a more direct metric of Cosmos damage since its time derivative is related directly to loading. We found that the $P_{coslt1} > P_{cosgt1}$ in all cases. Also, $\frac{P_{coslt1}}{m_{coslt1}} > \frac{P_{cosgt1}}{m_{cosgt1}}$ for all cases, signifying that most momentum is focused in the lower fraction of mass (in small debris). E_{loss} is the most direct damage metric, as it is the energy lost due to irreversible processes such as plasticity, fracture, as well as pressure-volume loading and release. E_{loss} correlated well with P_{coslt1}, another damage metric. The partitioning of mass, momentum, and energy in the collision debris, particularly the smaller debris, has important implications on the development of collision debris mass and velocity distribution models.

Table 3. Predicted Cosmos debris mass (m), momentum (P), and kinetic energy (KE) for debris greater than and less than 1 cm in size (denoted by subscript cosgt1 and coslt1). Also includes energy losses (E_{loss}). Reported as a % of the initial Cosmos mass (898 kg), initial system momentum (6.73E+06 kg-m/s), and initial system kinetic energy (3.92E+07 kJ) with respect to fixed reference frame of the Cosmos. Momentum is in the direction parallel to initial velocity (momentum) vector of Iridium.

Scenario	m_{cosgt1} *(%)*	m_{coslt1} *(%)*	P_{cosgt1} *(%)*	P_{coslt1} *(%)*	KE_{cosgt1} *(%)*	KE_{coslt1} *(%)*	E_{loss} *(%)*
GB1	82.02	17.98	0.33	1.80	<0.01	0.76	1.82
GB2	96.43	3.57	0.10	0.57	<0.01	0.28	0.50
GB3	93.95	6.05	0.08	0.21	<0.01	0.07	0.23
GB4	94.42	5.58	0.08	0.29	<0.01	0.10	0.32
MO	41.18	58.82	0.37	13.50	<0.01	11.83	7.96

Iridium-sphere collision modeling results

Figure 4 shows the progression of Iridium-sphere collision simulations for 10 cm radius aluminum sphere at 5 and 15 km/s closing velocity. Simulations were performed in reference frame fixed to Iridium, with the initial velocity vector given to the spherical projectile. In all simulations, the sphere impacts the center of the Iridium. Specifically, the sphere impacts the communications panel and, subsequently, the particles impact the bus. For all cases, the damage is rather diffuse due to the cascading debris mechanism discussed earlier. At 1 ms, the extent of damage zones in the communications panel and bus is much more significant in the 15 km/s than in the 5 km/s case. At 9 ms, the difference in the satellite damage for the different closing velocities is very evident, with more significant damage occurring with larger closing velocities. After 9 ms, the metrics associated with continued debris generation, relative debris velocity or velocity gradients within individual debris pieces, are generally small and not sufficient to create new debris.

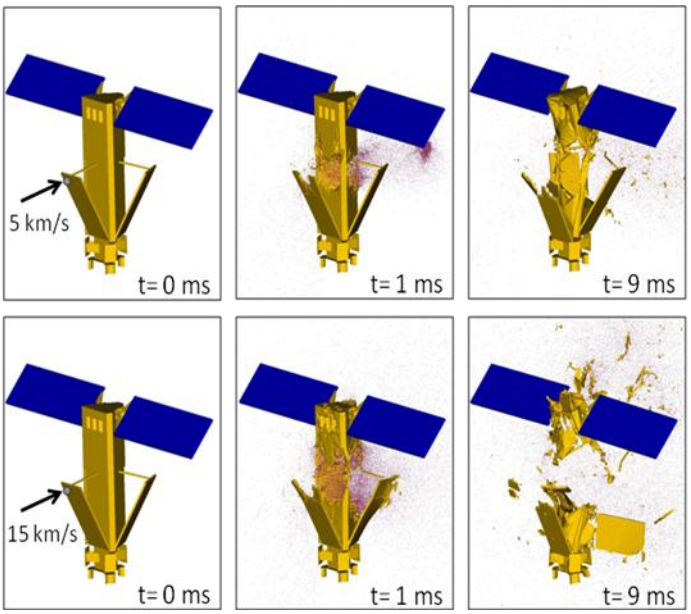

Figure 4. Progression of Iridium-sphere collision simulations for 10 cm radius aluminum sphere at velocities of 5 and 15 km/s. Newly created SPH particles are shown in red.

Figure 5 shows the predicted Iridium cumulative debris length distribution due to impact by 5 and 10 cm radius spherical projectile at velocities of 5, 10, and 15 km/s. We found that the total number of fragments, increasing from 144 to 1039, and the cumulative debris length distributions tend to scale with increasing initial projectile momentum. In general, the cumulative debris length distribution obeys a power-law trend ($N_{cum} = aL^b$). We performed a least squares fit to determine the power-law parameters. The fitted power-law parameters and other debris statistics are shown in Table 3. There is a transition in the cumulative length distribution at lower N_{cum} (<10), which corresponds to a length of 1 m. The transition is similar to those observed in the Iridium-Cosmos collisions. So, we also fit the cumulative debris length distribution curve above this transitional value. For these cases, the range of the power-law slope, b, for the higher N_{cum} (-0.862 to -1.135) are steeper than those for the overall curve (-0.603 to -1.13). The power-law slope, b, increases with increasing projectile momentum for both the overall curve and the higher N_{cum} .

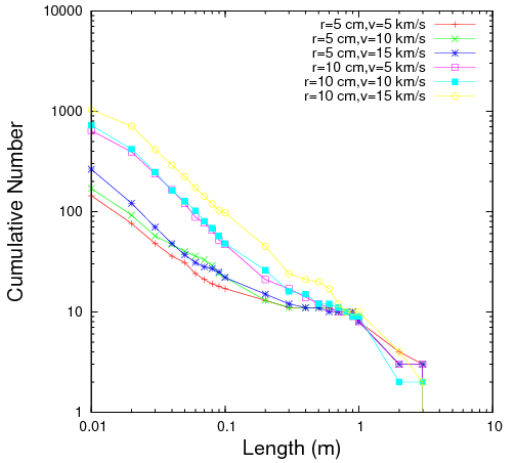

Figure 5. Predicted Iridium cumulative debris length distribution due to impact by 5 and 10 cm radius spherical projectile at velocities of 5, 10, and 15 km/s.

Table 4. Predicted Iridium debris statistics for debris size greater than 1cm. Includes number of fragments (N_{tot}), average power-law fit parameters (a_{avg}, b_{avg}) and power-law fit parameters for only large N_{cum} (>10) (a_{hi}, b_{hi}) for 5 and 10 cm radius spherical projectile at velocities of 5, 10, and 15 km/s.

Projectile Radius and Velocity	N_{tot}	a_{avg}	b_{avg}	a_{hi}	b_{hi}	V_0 *(m/s)*	n_v
5 cm, 5 km/s	144	5.73	-0.60	2.39	-.86	95.4	-0.02
5 cm, 10 km/s	170	5.70	-0.68	3.22	-.85	197.4	-0.03
5 cm, 15 km/s	264	5.56	-0.72	2.23	-.99	95.8	-0.01
10 cm, 5 km/s	642	6.02	-1.00	3.58	-1.16	910	-0.01
10 cm, 10 km/s	726	5.70	-1.04	3.71	-1.17	1092	-0.01
10 cm, 15 km/s	1039	7.38	-1.13	7.05	-1.14	1572	-0.01

Figure 6 shows the predicted Iridium cumulative debris velocity distribution due to impact by 5 and 10 cm radius spherical projectile at 5, 10, and 15 km/s. Velocities are relative to the fixed Iridium frame-of-reference. The cumulative debris velocity distribution curves generally increase for increasing initial projectile momentum. The velocity distribution curves obeys an exponential relationship, $N_{cum} = V_0 e^{n_v V}$. Table 4 lists the exponential model parameters. The velocity prefactor, V_0, increases with increasing initial projectile momentum except in the 5 cm radius-15 km/s case. In this higher velocity case, the highest velocity fragments tend to cause curve fits to reduce the velocity prefactor. The exponential power, n_v, shows little correlation with initial projectile momentum or velocity.

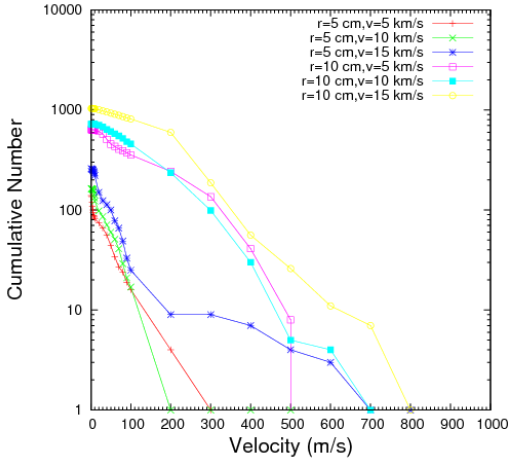

Figure 6. Predicted Iridium cumulative debris velocity distribution due to impact by 5 and 10 cm radius spherical projectile at 5, 10, and 15 km/s. Velocities are relative to the fixed Iridium frame-of-reference.

The predicted Iridium debris mass, momentum, and kinetic energy for debris greater than and less than 1 cm in size are shown in Table 5. We found that the $\mathrm{m_{iridlt1}}$ increased with increasing $\mathrm{P_{proj}}$ and KE_{proj}. Since the CM overlap is fixed in these simulations for each the 5 and 10 cm radius, it is expected that the small debris and other damage metrics would scale with initial projectile momentum or kinetic energy. As with the Iridium-Cosmos collisions, the momentum in the smallest debris $\mathrm{P_{iridlt1}}$ is significantly higher than in the larger debris, $\mathrm{P_{iridgt1}}$. We also found that the 5 cm projectile more efficiently transferred momentum to the Iridium (30.78 to 38.65% of initial projectile momentum) than the 10 cm projectile (20.66 to 28.71%). This suggests that eight 5 cm debris objects with sufficient spacing can impart more momentum, thus damage, than one 10 cm debris object at the same velocity. E_{loss} is the most direct damage metric, as it is the energy lost due to irreversible processes such as plasticity, fracture, as well as pressure-volume loading and release. E_{loss} correlated well with $P_{iridlt1}$, another damage metric. The partitioning of mass, momentum, and energy in the collision debris, particularly the smaller debris, has important implications on the development of collision debris mass and velocity distribution models.

Table 5. Predicted Iridium debris mass (m), momentum (P), and kinetic energy (KE) for debris greater than and less than 1 cm in size (denoted by subscript $\mathrm{iridgt1}$ and $\mathrm{iridlt1}$). Also includes energy losses (E_{loss}). Reported as a % of the initial Iridium mass (577 kg), projectile momentum, and projectile kinetic energy. The initial projectile momentum and kinetic energy are also listed. Momentum is in direction parallel to initial velocity (momentum) vector of projectile. Simulations were performed in the fixed reference frame of the Iridium.

Scenario	$m_{iridgt1}$ *(%)*	$m_{iridlt1}$ *(%)*	P_{proj} *(kg-m/s)*	$P_{iridgt1}$ *(%)*	$P_{iridlt1}$ *(%)*	KE_{proj} *(kJ)*	$KE_{iridgt1}$ *(%)*	$KE_{iridlt1}$ *(%)*	E_{loss} *(%)*
5 cm, 5 km/s	99.04	0.96	6.87E3	10.00	20.78	1.72E4	0.02	9.61	34.58
5 cm, 10 km/s	98.05	1.95	1.37E4	7.81	30.84	6.87E4	0.02	13.94	38.06
5 cm, 15 km/s	97.34	2.66	2.06E4	6.29	30.00	1.55E5	0.02	12.94	36.76
10 cm, 5 km/s	97.32	2.68	7.50E4	5.55	15.11	1.88E5	0.09	8.81	22.92
10 cm, 10 km/s	95.03	4.97	1.50E5	3.98	21.41	7.50E5	0.03	13.84	24.85
10 cm, 15 km/s	91.92	8.08	2.25E5	3.50	25.21	1.69E6	0.02	11.56	24.07

Figure 7 shows the normalized total number of debris ($\frac{N_{tot}(P)}{N_{tot,ref}}$) and normalized velocity prefactor ($\frac{V_0(P)}{V_{0,ref}}$) as function of normalized initial projectile momentum ($\frac{P}{P_{ref}}$). We developed momentum-based scaling relationships for these quantities:

$$\frac{N_{tot}(P)}{N_{tot,ref}} = \left(\frac{P}{P_{ref}}\right)^{\mathrm{n_{npnorm}}} \quad (9)$$

$$\frac{V_0(P)}{V_{0,ref}} = \left(\frac{P}{P_{ref}}\right)^{\mathrm{n_{vpnorm}}} \quad (10)$$

For these relationships, reference values for the total number of debris ($N_{tot,ref}$), velocity prefactor ($V_{0,ref}$), and initial projectile momentum ($V_{0,ref}$) were based on the 5 cm-5 km/s case. The only variable is the initial projectile momentum, P. The power-law exponents, $\mathrm{n_{npnorm}}$ and $\mathrm{n_{vpnorm}}$, are 0.62 and 0.89, respectively. In conjunction with assumptions about the debris size and velocity distributions, these momentum-scaling relationships enable the development of predictive models for the satellite-projectile and satellite-satellite debris.

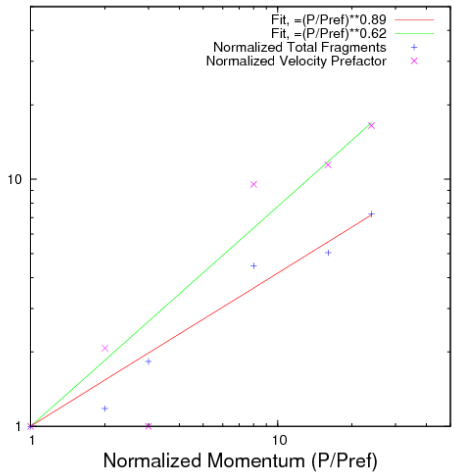

Figure 7. Momentum-Scaling of the Iridium Total Debris (> 1cm) and the Debris Velocity Prefactor.

CONCLUSIONS

- Our hybrid FEA-SPH code enabled us to investigate the influence of CM overlap and orientation, debris size, and relative velocity on the collision debris size and velocity distributions, as well as mass, momentum, and energy partitioning
- Two separate damage modes were observed in the Iridium-Cosmos collision simulations. The first mode is best described as diffuse, cascading damage. This diffuse damage is due to the successive creation of debris from the initial impact location and continuing downstream through thin, multi-layered structures. This type of debris formation is responsible for the smaller debris and is most similar to the intrinsic, "natural" fragmentation of different materials [5-7]. The second damage mode can be described as a shear mode with little or no diffuse damage. It occurs with the impact of single-layered structures. The resultant debris from this initial impact does minimal damage to surrounding structure and thus there is no cascading debris mechanism. This latter damage mode was responsible for the formation of the largest debris in GB1, the Iridium solar panel and Cosmos gravity boom remnants (see Figure 2). Since the formation of debris in this mode is somewhat deterministic, i.e., depends largely on the satellite and collision geometries, its prediction lends itself to graphical visualization and analysis tools.
- The cumulative Cosmos debris size distribution obeyed a power-law trend for the Iridium-Cosmos collisions. However, there are distinct features of the distribution above and below a debris number of 10. Below this threshold, the debris tends to have been formed via the shear damage mode and is largely dependent on collision geometry uncertainties. We attempted to bound the uncertainties by exploring several different collision geometries. Above this threshold, the debris tends to have been formed via the diffuse damage mode.
- Satisfactory agreement was demonstrated between the prediction of total debris for GB1 scenario and Liou's RCS-based data [10]. *This suggests that the Iridium-Cosmos collision was likely a low CM overlap*

event rather than a high CM overlap event where several thousands of debris objects would be expected. Comparison with overall RCS-based curve suggests that the smallest debris predictions for all simulations are too widely distributed in size. However, the underlying assumptions of the predicted debris size (i.e., bounding box algorithm utlized) and the debris RCS-to-size need to also be revisited.

- The partitioning of Cosmos mass, momentum, and energy for the Iridium-Cosmos collisions yielded interesting insights. The mass of small debris (<1 cm), the momentum transferred to the Cosmos, and the energy losses are all good metrics of damage in simulations. Most of the momentum and kinetic energy transferred to the Cosmos were in the small debris, which is less likely to be observed during collision and may re-enter after the collision. It is important to understand this mass, momentum, and energy partitioning in the overall debris in order to develop predictive models for the largest debris (>1 cm).
- In the Iridium-sphere collision simulations, we mainly observed the diffuse damage mode. However, due to the size of the projectile, there were still large debris remnants from the collisions. As with the Iridium-Cosmos collisions, the Iridium debris size distribution obeyed a power-law trend. The slope and total number of fragments predicted scaled with initial momentum of the sphere. The debris velocity distribution obeyed an exponential trend and the velocity prefactor also scaled with initial momentum of the sphere.
- The partitioning mass, momentum, and energy in the Iridium debris yielded similar results to the Iridium-Cosmos predictions. The mass of small debris (<1 cm), the momentum transferred to the Iridium, and the energy losses are all good metrics of damage. Also, most of the momentum and kinetic energy transferred to the Iridium were in the smallest debris. In investigating the effects of projectile size, we found that the 5 cm projectile more efficiently transferred momentum to the Iridium than the 10 cm projectile. This suggests that eight 5 cm debris objects with sufficient spacing can impart more momentum, thus damage, than one 10 cm debris object at the same velocity.
- The Iridium total debris and the debris velocity prefactor were found to scale with momentum and we developed a power-law relationship. This model is an initial step at developing predictive models for the collision debris size and velocity distribution based on high-fidelity simulations.

ACKNOWLEDGEMENTS

This work performed under the auspices of the U.S. Department of Energy by Lawrence Livermore National Laboratory under Contract DE-AC52-07NA27344.

REFERENCES

1. Kessler, D.J., Cour-Palais, B.G., "Collision Frequency of Artificial Satellites: The Creation of a Debris Belt", *Journal of Geophysical Research* 83, pp. 63, 1978.
2. Lin, J.I., "DYNA3D: A nonlinear, explicit, three-dimensional finite element code for solid and structural mechanics", *LLNL Report UCRL-MA-107254*, 2005.
3. Morris, J.P., "Analysis of smoothed particle hydrodynamics with applications", *Monash University, Melbourne, Australia, PhD Thesis*, 1996.
4. Moss, W.C., Levatin, J.L., "MOSSFRAC: An anisotropic 3D fracture model", *LLNL Report UCRL-TR-223712*, 2006.
5. Mott, N.F., "Fragmentation of Shell Cases", *Proc. Roy. Soc. Lond. A*, 189, pp. 300-308, 1947
6. Grady, D.E., Kipp, M.E., "Continuum Modelling of Explosive Fracture in Oil Shale", *Int. J. Rock Mech. Min. Sci & Geomech. Abstr*., 17, pp. 147-157, 1980
7. Grady, D.E., "Fragmentation of Solids Under Impulse Stress Loading*", Journal of Geophysical Research* 86, pp. 1047-1054, 1981
8. Steinberg, D. J., "Equation of state and strength properties of selected materials" *LLNL Report UCRL-MA-106439*, 1996.
9. Levatin, J.L., Springer, H.K., Moss, W.C., "DFRAG: A DYNA3D fragment postprocessor", *LLNL Report UCRL-SM-217992*, 2006.
10. Liou, J.-C., "An update on recent major breakup fragments", *NASA Orbital Debris Quarterly News*, Volume 13, Issue 3, July 2009.
11. Har-Peled, S., "A practical approach for computing the diameter of a point-set", *Proceedings of the Seventeenth Annual Symposium on Computational Geometry*, June 3-5, 2001, Medford, MA, USA. ACM, pp. 177-186, 2001